Molecular-dynamics study of Poiseuille flow in a nanochannel and calculation of energy and momentum accommodation coefficients

Sooraj K. Prabha and Sarith P. Sathian*

Computational Nanotechnology Laboratory, National Institute of Technology Calicut, Kozhikode-673 601, Kerala, India

(Received 6 September 2011; revised manuscript received 17 February 2012; published 16 April 2012)

We report a molecular-dynamics study of flow of Lennard-Jones fluid through a nanochannel where size effects predominate. The momentum and energy accommodation coefficients, which determine the amount of slip and temperature jumps, are calculated for a three-dimensional Poiseuille flow through a nano-sized channel. Accommodation coefficients are calculated by considering a " gravity"- (acceleration field) driven Poiseuille flow between two infinite parallel walls that are maintained at a fixed temperature. The Knudsen number (Kn) dependency of the accommodation coefficients, slip length, and velocity profiles is investigated. The system is also studied by varying the strength of gravity. The accommodation coefficients are found to approach a limiting value with an increase in gravity and Kn. For low values of Kn (<0.15), the slip length obtained from the velocity profiles is found to match closely the results obtained from the linear slip model. Using the calculated values of accommodation coefficients, the first- and second-order slip models are validated in the early transition regime. The study demonstrates the applicability of the Navier-Stokes equation with the second-order slip model in the early transition regime.

DOI: 10.1103/PhysRevE.85.041201 PACS number(s): 47.61.−k

I. INTRODUCTION

Gas flow in micro- and nanochannels frequently falls into the slip or in the early transitional regime. It is now known that for fluid flow through micro- and nanochannels, where the characteristic dimension is of the order of the mean free path of molecules, the continuum assumptions are no longer valid [1]. In the development of potential applications such as microelectromechanical and nanoelectromechanical systems (MEMS and NEMS), for example, micropumps, microturbines, and portable gas chromatography systems, we encounter the phenomenon of noncontinuum flow. Accurate predictions regarding the thermophysical aspects of noncontinuum flow are the main challenges in the design, development, and fabrication of such systems. The direct measurement of gas-surface interaction parameters in a nanochannel is difficult to perform and demands complex instrumentation. However, there have been many important experimental studies on gas-surface interaction parameters of high-Knudsen-number (Kn) flow, especially through microchannels [2–5]. Furthermore, researchers have used a variety of molecular-based numerical schemes to analyze high-Knudsen-number flows [6–11].

The use of the Navier-Stokes (NS) equation can be extended to the slip regime by using the appropriate boundary conditions as demonstrated in several studies [12–14]. There have been attempts to further extend the validity of the NS equation to pressure-driven flows, with higher-order slip and temperature jump boundary conditions [4,5]. Colin *et al*. have summarized the main theoretical and experimental works of such pressure-driven flows [15]. The momentum and energy accommodation coefficients are the important parameters governing the amount of slip and temperature jumps occurring at the surface. These gas-solid interaction properties are sensitive to many factors, such as gas-solid pairs, surface temperature, absorbents, lattice configurations, and surface roughness [16]. Inasmuch as the slip occurs at the boundary on a scale of the order of the mean free path, it is difficult to measure it experimentally. This gives extreme importance to molecular-based numerical simulations to replace experiments in such regimes. Among such numerical schemes, the molecular-dynamics (MD) method is considered an accurate numerical method to analyze gas-surface interactions at the micro and nano scales [17].

A majority of different numerical modeling approaches to analyze slip flow assume diffuse wall boundary conditions or calculate accommodation coefficients (ACs) indirectly. In this study, the accommodation coefficients of the Poiseuille flow are calculated directly and are used to analyze the slip phenomenon. Many investigators have simulated the pressure-driven flow of gases [18–20] and liquids [21,22] through a microchannel by applying an acceleration field (gravity, g) to the fluid molecules. In this work, the accommodation coefficients are calculated for a gravity-driven Poiseuille flow in a nanochannel.

The ACs for fluid flow through a nanochannel are investigated using MD. The walls of the nanochannel, modeled as parallel and infinite, are maintained at a common fixed temperature. The calculated values of accommodation coefficients are used to obtain the dimensionless slip lengths for the Maxwell slip model and are compared with the slip length obtained from the velocity profiles. In the transition regime, the first- and second-order linear slip models are validated using the calculated values of accommodation coefficients. The method described in this study can be used to obtain information about the gas-surface interaction properties of a gravity-driven flow.

II. ACCOMMODATION COEFFICIENTS

The accommodation coefficient is a measure to quantify the interaction between a wall and a fluid. It indicates the degree to which molecules are accommodated to the surface. The energy accommodation coefficient (EAC) is a measure to account for

*sarith@nitc.ac.in

the thermal accommodation during the gas-solid interaction. The EAC can be defined as

$$\alpha_E = \frac{\bar{E}_i - \bar{E}_r}{\bar{E}_i - E_w}, \tag{1}$$

where E denotes energy and i and r denote the incident and reflected conditions, respectively. The subscript w denotes the wall surface and the quantities with w are determined from thermal wall distributions, which are constants for a given wall temperature [23]. The momentum accommodation coefficients are defined to analyze and measure the momentum transferred to the solid surface during the scattering process. The AC based on the tangential component of momentum is defined as

$$\alpha_t = \frac{\bar{p}_{ti} - \bar{p}_{tr}}{\bar{p}_{ti}}, \tag{2}$$

where t denotes the tangential direction to the solid surface and p is the momentum. The AC based on the normal component of velocity is given as

$$\alpha_n = \frac{\bar{p}_{ni} - \bar{p}_{nr}}{\bar{p}_{ni} - p_w}, \tag{3}$$

where n denotes the direction normal to the surface. The absolute values of normal momentum are considered for the calculation of the normal momentum accommodation coefficient (NMAC), for which the calculated values are expected to be in between 0 and 1 [24]. In addition, this definition is consistent with that of EAC and it would render values that are comparable with EAC.

III. SIMULATION MODEL

A. Wall model

Modeling of the wall is of central interest in the study of gas-surface interactions and is one of the challenging problems in this field. The wall models can be broadly divided into stochastic models [25,26] and solid wall models. Solid wall models have evolved over the years from the early lattice models that are capable of incorporating nonzero surface temperatures [27,28]. Models such as the rigid lattice model [29], heavy walls [30], the phantom wall model [31], and the Einstein wall model [14,32] show the diversity of such wall models. The explicit wall model is used for the present study [23,33]. It considers the interactions with neighboring atoms within a cut-off distance. This is essential to retain the structural integrity of the solid and to properly define the solid-solid interaction. For modeling a 3D solid surface with nonzero surface temperatures, the explicit wall model is the best suited among the wall models discussed here.

B. Details of simulation

A three-dimensional system in which a monatomic gas (argon) flows between infinite parallel surfaces (platinum) is opted for the study. Platinum is modeled as a "model surface," which is assumed to be smooth and clean and without any defects. For the system studied in the present case, the rarefaction levels of the gas are in the slip and early transition regime.

The dimensions of the simulation box are chosen to be $10 \times 12 \times 10$ nm. The direction normal to the solid surface is the y direction and the flow is in the positive x direction. (Fig. 1). The smallest dimension of the simulation box is kept greater than or equal to the characteristic dimension of the system. The total number of atoms in the simulation is around 20 000, of which 18 928 are wall atoms. Initially, the atoms are arranged in an FCC structure for the solid and in a random configuration for the gas.

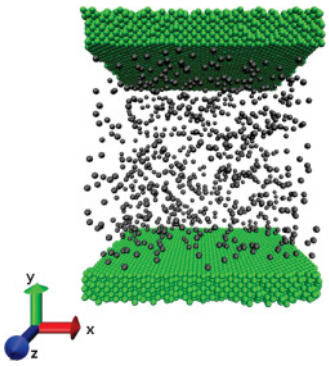

FIG. 1. (Color online) Perspective view of the simulation model. The dimensions of the simulation box are $10 \times 12 \times 10$ nm. The gas flow is in the positive x direction.

The interactions are modeled using the Lennard-Jones (LJ) potential with a cut-off distance equal to 2.5 times the LJ length parameter [17]. The cut-off distance is selected by considering mainly the force field strength, rarefaction levels, the accuracy of parameters calculated, and the computational cost associated with it. The data reported in the recent studies are used in this simulation. The characteristic length parameters for the LJ potential are chosen to be 0.340 and 0.247 nm for argon and platinum, respectively [23]. The interaction strength for the model is taken as 31.36 kJ/mol for the Pt-Pt interaction and 0.996 kJ/mol for the Ar-Ar interaction [34]. For solid-solid interactions, an adequately high value of the interaction potential along with temperature control is essential to retain the structural integrity of the solid. We take 0.658 kJ/mol for the Pt-Ar interaction for the characteristic LJ length of 0.294 nm [23,35]. The mass of argon is 39.95 amu and that of platinum is 195.1 amu.

Periodic boundary conditions are employed in all directions. The two walls are located at the extremes. The periodic boundary condition in the xz direction ensures the infinite parallel wall assumption. The total simulation run is divided into two parts, the equilibration and production run. Velocity-Verlet algorithm is used for the integration. To control the heat produced in the walls due to collisions and to maintain the wall temperature, thermostats are applied on both walls. Temperature of the wall is maintained at 300 K using a Berendsen thermostat by controlling translational degrees of freedom of the wall atoms [36]. To eliminate any unbalanced force, the velocity of the center of mass of the system is made zero at frequent intervals without altering the relative positions of the atoms. Parallel algorithms for classical molecular dynamics are used for implementing MD simulations with short-range forces [37]. Visualization was implemented using Visual Molecular Dynamics (VMD) (Fig. 1) [38].

C. Tracking of collisions

Collisions are tracked by defining a plane near the wall. When the atoms cross the plane, collisions are recorded [14,20,23]. When an atom crosses the plane toward the wall, the incident components of collision are recorded and when the atom cross the plane away from the wall, the reflected components are recorded. The incident components and reflected components together constitute a collision. The location of the plane is determined by considering the influence of the wall on a gas atom and the mean free path of the gas atoms. In the present study, the gas is so rarefied that the possibility of collisions with another gas molecule near the wall is rare. The location of the collision tracking plane is fixed to be at a wall-gas interaction cut-off distance.

IV. SLIP MODELS

It is well established that there exists a considerable amount of relative velocity at the wall-gas interface of low density flows, which is known as slip. Over the years there have been many attempts to model and quantify these slip effects. It was Navier who pointed out that a fluid might slip on a solid surface and who introduced the concept of slip length to quantify the slip boundary condition. The slip velocity is given as

$$v_{sN} = L_s\left(\frac{dv_x}{dy}\right)_w, \tag{4}$$

where v_s is the slip velocity, v_x is the component of velocity in the x direction, and L_s is the slip length. The slip length L_s for the Navier model can be obtained from velocity profiles by extrapolating the slope of it to zero velocity [11,16].

Maxwell assumed that half of the molecules near the boundary are moving away from the wall and the other half are heading toward the wall. From the model, we obtain that the slip velocity is proportional to the mean free path and velocity gradient along the normal to the surface [1]. It takes the following form:

$$v_{sM} = aC_1\lambda\left(\frac{dv_x}{dy}\right)_w, \tag{5}$$

where a is the constant of proportionality, which is often approximated to unity. The Maxwell model takes $C_1 = (2 - \alpha_x)/\alpha_x$. In this model, which is a first-order linear slip model, the velocity slip is proportional to the mean free path and velocity gradient, and, hence, the relation is linear.

Second-order linear slip models generally take the following form:

$$v_s = C_1\lambda\left(\frac{dv_x}{dy}\right)_w - C_2\lambda^2\left(\frac{d^2v_x}{dy^2}\right)_w, \tag{6}$$

wherein C_1 and C_2 are first- and second-order slip coefficients, respectively. C_2 is zero for first-order linear slip models. Second-order slip models are mostly based on the Maxwell model.

V. RESULTS AND DISCUSSION

In a nanochannel, Poiseuille flow can be realized either by applying a constant acceleration field in the flow direction or by setting a suitable boundary condition in the flow direction to create a pressure gradient. In this study, a computationally efficient method of providing an acceleration field is employed to maintain a nonequilibrium flow in the x direction. The pressure drop along the flow direction is assumed to be a constant for the selected length scale.

Different flow conditions are realized in the channel by varying the strength of gravity. The order of magnitude of the applied gravity is several times larger than that of acceleration due to gravity. The production run (1–2 ns) starts after the system attains steady state. Since the system is analyzed with different flow conditions, the optimum time step will differ for different conditions. It was identified, by use of trial and error, that the step length has to be in a range of 1 to 2 fs. In the present study, a step length of 1 fs is used. Unless specified, the results for gravity $g = 5 \times 10^{-7}$ nm/ps^2 are used for demonstration.

The rarefaction level in the channel is varied by varying the number of gas atoms from 3072 to 272. The kinetic theory equation for the Knudsen number for the hard sphere model has been used to calculate Kn. The mean free path is approximated as $\lambda = \sqrt{2}\pi d^2 n$, where d is the diameter of the gas atom and n is the number density [19,23]. When a continuous potential field like the LJ potential is present, the path length between collisions varies with position. As the present study is concentrated at higher rarefaction levels (transition regime), the effect of attractive potential fields will be weak in the bulk fluid and the kinetic theory expression for the mean free path can give a good estimate of the mean free path. The Knudsen number thus calculated is used to characterize the flow conditions.

A. Single-particle trajectories

Analysis of the motion of individual atoms provides further insight into Poiseuille flow. The fluid atoms will have random as well as drift motion. The structural integrity of the wall is also crucial as it affects the scattering process. Atoms are randomly selected from the solid wall and the fluid and the trajectories are tracked for a duration of 100 000 time steps. The orthographic view of single-particle trajectories are shown in Fig. 2. The solid lines represent the solid wall

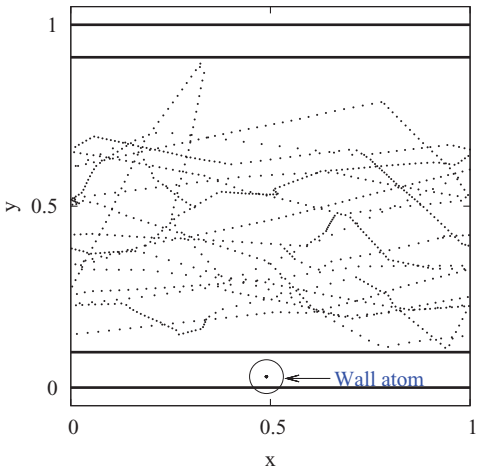

FIG. 2. (Color online) Single-particle trajectories for the wall and the fluid atoms. The solid lines represent the solid wall boundaries. The trajectories are of a single atom in the wall and the fluid. The wall atom trajectory is highlighted with a circle.

TABLE I. Calculated values of accommodation coefficients are given. The standard deviation of the entries is given in parenthesis. The value of g is in nm/ps^2.

Case	$g \times 10^7$	α_x	α_y	α_z	α_E
			Kn = 0.07		
1	5	0.401(0.004)	0.097(0.005)	0.809(0.006)	0.214(0.001)
2	30	0.273(0.001)	0.049(0.002)	0.757(0.003)	0.175(0.003)
3	50	0.274(0.001)	0.018(0.002)	0.753(0.003)	0.162(0.001)
			Kn = 0.39		
4	5	0.307(0.004)	0.090(0.007)	0.399(0.007)	0.221(0.005)
5	30	0.196(0.003)	0.065(0.002)	0.321(0.007)	0.152(0.003)
6	50	0.190(0.002)	0.050(0.003)	0.324(0.004)	0.143(0.002)
			Kn = 0.72		
7	5	0.290(0.004)	0.096(0.006)	0.313(0.007)	0.218(0.006)
8	30	0.178(0.003)	0.071(0.004)	0.241(0.007)	0.143(0.003)
9	50	0.172(0.003)	0.055(0.002)	0.247(0.005)	0.135(0.002)

boundaries. Clearly, as seen from the figure, the solid atom has no drift motion and retains its position, thus providing structural integrity to the solid surface. The fluid atoms are having random as well as ordered motion. In addition, we observe that there is no binding of fluid atoms to the wall for the selected gravity field.

B. Accommodation coefficients

In the present study, ACs are defined and calculated for average incident and reflected properties. The selected values (two extreme values and an intermediate value) of ACs are tabulated in Table I. To determine the statistical scatter of calculation, the collision data are divided into an equal number of classes (8). The class averages yield ACs and the standard deviation of ACs thus obtained from different classes is given in brackets. The overall value of standard deviation is low, indicating the stability of the calculated values. It is observed that nearly 100 000 collisions are sufficient to obtain a statistically stable calculated value. The applied gravity is in the range of 5 to 50 $\times$ 10^{-7} nm/ps^2. The procedure is repeated for different Knudsen numbers ranging from 0.065 to 0.721.

1. Tangential momentum accommodation coefficient (TMAC)

To calculate TMAC, the incident direction is taken as positive, irrespective of the direction of incidence, and, if the direction changes on collision, it is taken as negative. The ACs are calculated as per Eq. (2). The variation of momentum accommodation in the flow direction with Kn and gravity is shown in Fig. 3. The value of AC in the flow direction is found to increase with a decrease in Kn and it can be presumed that the value of AC will monotonically increase and approach unity for lower values of Kn. This is in good agreement with the result reported by Maurer *et al.* for the measurement of TMAC for gas flow through a microchannel [5]. In addition, the values of the ACs decrease and tend to attain a limiting value with an increase in gravity. This trend agrees with the reported reduction in AC with increase in the drift velocity as the collisions occur at glancing angles [20].

The mean velocity of atoms in the z direction is found close to zero. With change in gravity and Kn, the ACs in the z direction show a homothetic behavior as in the x direction (Fig. 4). The calculated values of momentum AC in the z direction are high when compared to flow direction. As the drift velocity in the z direction is zero, the chances of reflection in the negative direction is high when compared to the flow direction.

The incident energy distribution for Case 1 (Table I) is calculated using the collision data (Fig. 5). The collision data contain the entire range of incident energy levels for all possible angles of incidence. The incident and reflected angles with respect to the normal to the surface are calculated for each collision. To gather information regarding the contribution of atoms at different energy levels, the data are sorted for a small range of angle of incidence $\theta_{\text{avg}} \pm \delta\theta$, where θ_{avg} is the average angle of incidence. The particles with different energy levels also mean that for each particle there is an associated " particle temperature." Collisions having this angle of incidence are segregated to different classes depending on the energy levels. Using this data, the TMAC is calculated and plotted against incident energy. To minimize statistical scatter in different classes, a large amount of collision data (2 million collisions) are considered for the calculation (Case 1).

For the collisions that happen at a fixed angle, the ratio of the tangential component of velocity to normal velocity

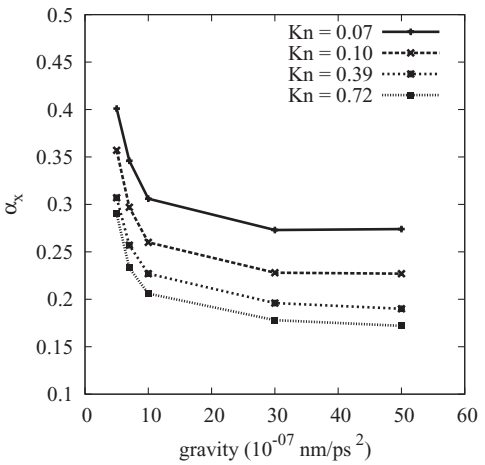

FIG. 3. Variation of partial momentum accommodation in flow direction (α_x) with Kn and gravity.

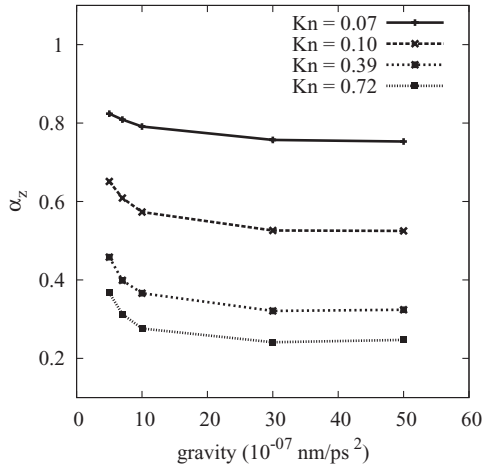

FIG. 4. Variation of the partial momentum accommodation in the z direction (α_z) with Kn and gravity.

is a constant. The tangential component of velocity in the x direction (v_x) has two parts, one that contributes to the thermal kinetic energy component and one that is a consequence of the imposed gravity field. The tangential momentum accommodation in the flow direction is dependent on the change in v_x on collision. For low values of energy, even if the thermal component is fully accommodated, due to the presence of gravity g, the molecule is more likely to continue in the same direction and yield a low value of α_x as per the definition. The presence of gravity decreases the chances of negative collision too. At higher energy levels, the significance of thermal component will be high and, hence, the value of α_x becomes greater. In addition, it brings down conditions that are favorable for full accommodation. Further increase in energy causes only marginal increase in α_x and the conditions that favor "reflection" will prevail over full accommodation. There exists an equilibrium condition between these two states, at which the ACs tends to attain a limiting value.

As seen from Fig. 5, the change in α_z with the change in energy is inconsistent with α_x. The momentum in the z direction accommodates well for lower values of energy as

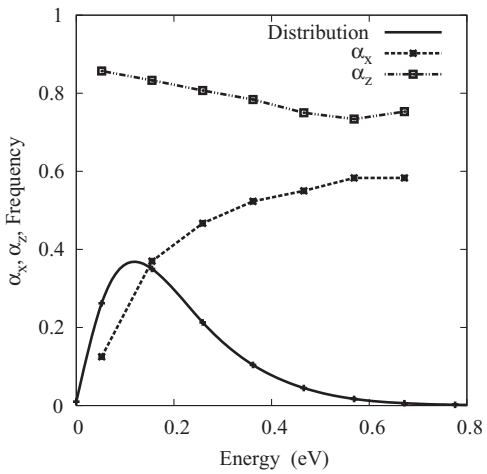

FIG. 5. Incident energy distribution and the variation of α_x and α_z with incident energy for mean angle of incidence.

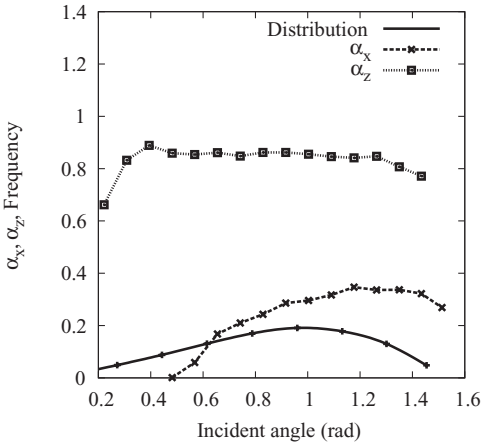

FIG. 6. Incident angle distribution and the variation of α_x and α_z with the angle of incidence for the mean incident energy.

it is free from the gravity term. As seen from the figure, at lower energies it accommodates momentum well and for higher values of energy it poorly accommodates. At higher values of energies, the conditions for "reflection" will prevail, and, hence, α_z decreases. On the other hand, α_x shows an increasing trend with an increase in energy. It can be presumed from the figure that for a sufficiently high value of the thermal component at the scattering conditions, both momentum components will tend to a limiting value.

A similar approach is adopted for studying the contribution of atoms with different angles of incidence (Case 1). The collisions with incident energy $E_{\text{avg}} \pm \delta E$, where E_{avg} is the average incident energy, are considered in this regard. As the energy is constant, the tangential component of velocity will vary with a change in the collision angle. Apparently, with an increase in the angle of incidence, α_x will increase followed by a subsequent decrease (Fig. 6). This is also due to the presence of gravity and the variation of the thermal component of velocity with angle of incidence. However, α_z has only a small influence on the angle of incidence except at the two extreme conditions.

2. *Normal momentum accommodation coefficient*

The value of NMAC, as per the definition, is expected in the range from 0 to 1 for a nonequilibrium molecular-dynamics simulation. As per the definition, the NMAC is dependent on wall temperature [Eq. (3)]. The value of NMAC is an order of magnitude lower when compared to other momentum accommodation coefficients (Table I). At higher acceleration fields, the atoms approach the solid surface at high angles, which effectively reduces the value of NMAC. The NMAC renders higher values if the angle of incidence is close to normal, provided the other parameters remain the same.

3. *Energy accommodation coefficient*

From the calculations, it is observed that the value of EAC varies inversely with gravity and Knudsen number. With an increase in gravity, the EAC consistently decreases and tends to attain a limiting value for the solid-gas system and further increases in gravity produce only marginal changes in EAC (Fig. 7). When the atoms possess high energy, the chances of

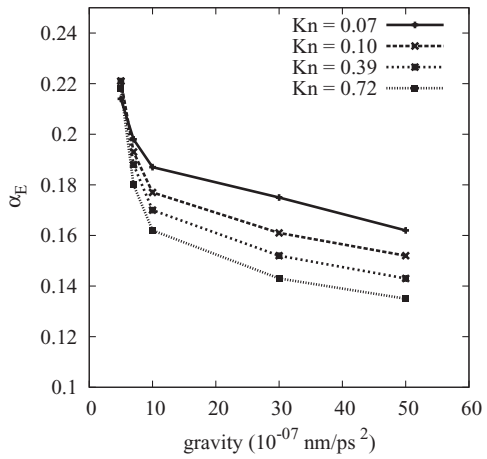

FIG. 7. Variation of energy accommodation coefficient (α_E) with Kn and gravity.

multiple collisions and physisorption are low. This reduces the chances of full accommodation. Our results agree well with the results of molecular beam simulations, where the dependence of EAC on surface temperature and angle of incidence was studied [39].

Under higher acceleration fields, the energy of the molecules is high, as are the velocities. This would affect the relaxation time and, consequently, the ACs (Fig. 8). To study this effect, the time spent by fluid particles in the interaction region (the region between the wall surface and the collision tracking plane) is calculated for different cases, shown in Table I. In Fig. 8, the time of interaction is plotted against the collision frequency. As seen from the figure, the energy accommodates well for higher interaction time.

C. Velocity profile, temperature profile, and slip length

1. Velocity profile

The velocity profile across the channel gives basic information about the microflow rarefaction effects. The velocity profiles for different rarefaction levels are depicted in Fig. 9. The dimensionless velocity component is plotted against

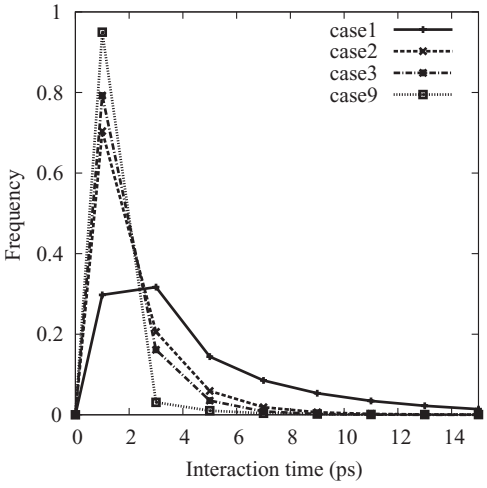

FIG. 8. Interaction time distribution for different cases.

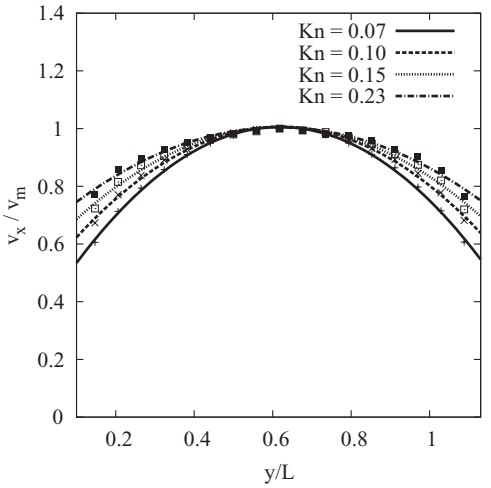

FIG. 9. The velocity profiles across the channel for different Kn are shown. The dimensionless velocity component is plotted against the dimensionless length parameter along the characteristic dimension.

the dimensionless length parameter across the stream. The velocities are scaled with maximum velocity and the length with the characteristic dimension. For a given g value, the velocity profile takes a parabolic form only for small Kn. As the rarefaction level increases, the profile straightens at the center and the slip velocity increases. The main difference among the velocity profiles is in the amount of slip observed at the wall-fluid interface. At lower densities, the collision rate will decrease and it augments the discontinuity near the wall.

2. Temperature profile

The variation of temperature of the fluid across the channel is another factor, which reflects the rarefaction effects in the microflow. The thermal kinetic energy components are used to calculate the temperature of the fluid. The calculated distributions are depicted in Fig. 10. When compared to velocity profiles, temperature profiles need larger amounts

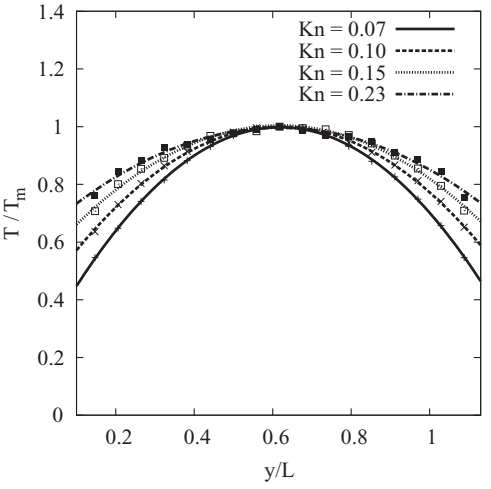

FIG. 10. The temperature profiles for different rarefaction levels are shown. The temperature profiles are normalized with the temperature of the bin that is located at the center of the channel.

of data to get a stable average value in a bin. Similarly to velocity profiles, the temperature profiles are normalized with the temperature of the bin that is located at the center of the channel. It is important to note that the discontinuity (temperature jump) observed near the wall increases with an increase in rarefaction levels and gravity. With an increase in rarefaction levels, the collision frequency at the gas-wall interface decreases and, hence, the discontinuity increases. For higher values of gravity, the interaction time will be small and, hence, the energy accommodated to the surface will decrease. Furthermore, as gravity increases, the molecules are more likely to continue in the same direction, which reduces the chances of collision. The effect of gravity on accommodation coefficients will be discussed in the later sections of this paper. The results of variation of the jump phenomenon with gravity are omitted for brevity.

3. Slip length

The dimensionless slip length is yet another parameter that characterizes the flow in the rarefied regime. The velocity profile obtained from MD simulation is used for the calculation of slip length for the Navier model. The dimensionless slip length is obtained as $l_s = L_s/L$, where L is the characteristic dimension of the flow. The effects of Kn and g on the slip length are considered here. The l_s shows a linear variation with the natural logarithm of Kn (Fig. 11) as reported by Battacharya [19]. It is observed that both the amount of slip and the slope of the velocity profile near the wall show a nonlinear variation with Kn. However, for a small range of Kn in the slip regime, these variations can be approximated to the linear variation. Additionally, the slip velocity varyies logarithmically with gravity for the range of g values discussed here (not shown). At lower values of Kn, the difference among slip lengths for different g values is scant.

According to the Maxwell model, the dimensionless slip length is related to the Knudsen number as follows:

$$l_{sM} = \frac{2-\alpha_x}{\alpha_x}\mathrm{Kn}, \tag{7}$$

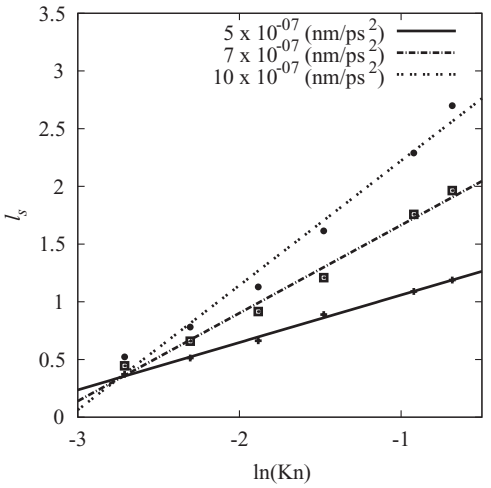

FIG. 11. The variation of dimensional slip length obtained from the velocity profile with Kn and g is shown. The least-squares linear fit lines are also shown.

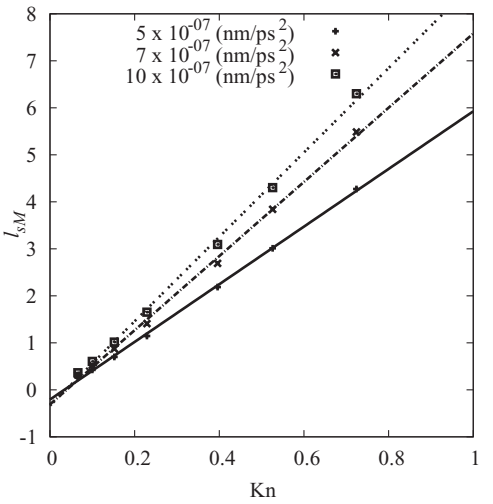

FIG. 12. Variation of dimensionless slip length for the Maxwell model (l_{sM}) with Kn and gravity. The calculated values of α_x are used to calculate l_{sM}. The least-squares linear fit lines are also shown.

where l_{sM} is the dimensionless slip length for the Maxwell model. The calculated values of ACs are used to predict the dimensionless slip length for the Maxwell model and it predicts a linear relationship between the slip length and Kn (Fig. 12). This is true for different g values, too. The values of the slip lengths for different g values converge at lower values of Kn. It indicates that for sufficiently lower values of Kn, the no-slip boundary condition can be employed, which is well known.

The slip length obtained from the Maxwell model (l_{sM}) is compared with the results from the velocity profiles (Fig. 13). The slip length changes in the same direction as g and Kn change for both slip models. The comparison shown in the figure indicates a similar qualitative trend for different g values. Moreover, the slip lengths closely match for low values of Kn and begin to deviate as Kn increases [40]. The variation of the Navier slip length is no longer linear with higher values of Kn (Fig. 11). This can be due to the nonlinear effects

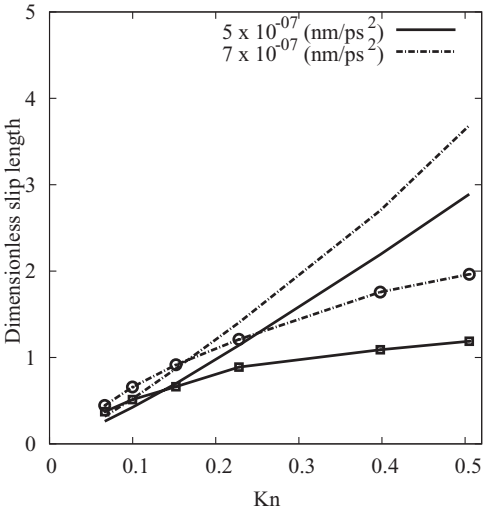

FIG. 13. Comparison of dimensionless slip lengths is shown. The lines represent the Maxwell model and the lines with points represent the Navier model.

near the walls at higher rarefactions, which have considerable influence on velocity distribution. However, for lower values of Kn (in slip regime), the variation of l_s with Kn can be approximated to a linear variation [32]. For a small range of Kn in this regime, assuming the value of TMAC is a constant in this range, both slip lengths can be compared to obtain TMAC from the velocity profiles. This reiterates the fact that the calculation of TMAC from velocity profiles using the Maxwell linear slip model is limited to low values of Kn.

In the kinetic theory model, the mean free path is assumed to be a constant along the characteristic dimension. It is now well known, from the numerous MD simulation studies of thermal problems, that the density distribution of the rarefied fluid phase near the wall shows oscillations [33,41]. This effect was not considered in the linear first-order slip model. The Maxwell model is based on the thermal equilibrium assumptions that break down at higher Kn. As the Kn increases, the nonequilibrium effects also increase in the Knudsen layer and sophisticated models are required to predict the slip phenomenon beyond the slip regime. Experimental studies have shown that the first-order models fail to predict the observed data for Kn $>$ 0.1 [4,5]. From the study of slip lengths, it is observed that the Maxwell model is capable of predicting the slip phenomenon accurately only for low values of Kn. This claim can be further validated by predicting the velocity distribution across the channel using linear slip models.

D. Velocity profiles using linear slip models

The velocity distribution for an isothermal flow in a long channel predicted by the second-order slip boundary condition is in the following form:

$$v_x(y) = -\frac{dP}{dx}\frac{L^2}{2\mu}\left[-\left(\frac{y}{L}\right)^2 + \left(\frac{y}{L}\right)\right] + v_s, \tag{8}$$

where dP/dx is the pressure drop, L is the characteristic dimension, and μ is the coefficient of dynamic viscosity [42]. The maximum velocity in the channel (v_m) will be the center line velocity. Normalising the flow velocity with the center line velocity, the equation takes the form:

$$\frac{v_x(y)}{v_m} = \frac{\left[-\left(\frac{y}{L}\right)^2 + \left(\frac{y}{L}\right) + C_1\mathrm{Kn} + 2C_2\mathrm{Kn}^2\right]}{\frac{1}{4} + C_1\mathrm{Kn} + 2C_2\mathrm{Kn}^2}. \tag{9}$$

This normalized form of velocity distribution is used to demonstrate the comparative study.

1. First-order slip model

In this section, the first-order linear slip model is validated in the early transition regime (Kn = 0.099–0.721). For the Maxwell model, the velocity profiles are predicted with Eq. (9), where $C_2 = 0$. There have been different values proposed for a depending on the different approaches used in kinetic theory [12]. To avoid ambiguity, in this study, the value of a is taken as 1.0. The values of center line velocities are taken from MD simulation data. The calculated values of TMACs are used for the calculation of slip velocity [Eq. (5)]. The predicted velocity profiles across the channel and its comparison with MD data are depicted in Fig. 14.

For lower values of Kn in the transition regime, the first-order slip model accurately predicts the velocity distribution. For a value of Kn $<$ 0.099 (not shown), the model slightly underpredicts the values obtained from MD. This is mainly because for two reasons: the unavoidable error that can happen in the calculation of Kn and TMAC at higher number densities. The validity of the kinetic theory model for calculating the mean free path is found to decrease at higher number densities. Furthermore, the mean free path is of the order of cut-off distance such that the possibility of gas-gas collisions in the collision region (region between the collision tracking plane and the solid surface) is high. This can affect the accuracy of calculated value of TMAC at lower Kn; as the cut-off distance is kept a constant for the entire range of simulation. On the other hand, at higher rarefaction levels, the effect of these possible errors mitigates and the first-order slip model fairly predicts the velocity distribution up to Kn = 0.15 [Fig. 14(b)]. Subsequent to the increase in Kn, the predicted distributions deviate further from the MD data, by over predicting the amount of slip. However, the higher-order slip model can be employed to predict the amount of slip beyond the effective limit of the first-order model.

2. Second-order slip model

As mentioned earlier, there have been many attempts to find the values of C_1 and C_2 in Eq. (6) such that the applicability of the NS equation can be further extended beyond the slip regime. In these studies the value of C_1 is found around unity and there is no general consensus on the value of C_2 [16]. Generally, C_1 is approximated to unity where rough surfaces are present or diffuse boundary conditions are imposed ($\alpha_x \sim 1$). Here, the calculated values of ACs are used to validate the second-order slip model.

For a pressure-driven flow, Beskok *et al.* [43] proposed a model for the velocity distribution across the channel as follows:

$$v_x(y) = -\frac{dP}{dx}\frac{L^2}{2\mu}\left[-\left(\frac{y}{L}\right)^2 + \left(\frac{y}{L}\right) + \frac{2-\alpha_x}{\alpha_x}(\mathrm{Kn}^2 - \mathrm{Kn})\right]. \tag{10}$$

The second-order slip model, when compared to Eq. (8), gives C_1 as $(2-\alpha_x)/\alpha_x$ and C_2 as $-(2-\alpha_x)/2\alpha_x$. The comparison of the second-order slip model with the MD data and the first-order model is depicted in Fig. 14. As seen from the figure, the second-order model shows better agreement with the results obtained from MD.

3. Discussion on velocity profiles using linear slip models

The applicability of these slip models can be validated by comparing the values of predicted average velocity and slip velocity with MD data. As seen from Fig. 14, subsequent to an increase in Kn, the amount of slip (the extreme points on both sides of the curve) predicted by the first-order model monotonically deviates from MD data. Even though the first-order model fails to predict the amount of slip, it fairly predicts the average velocity. For Kn $>$ 0.1, the second-order model predicts both the slip and average velocity with a good degree of accuracy. The percentage of deviation of slip velocity from the MD data is less than 5% for the second-order model,

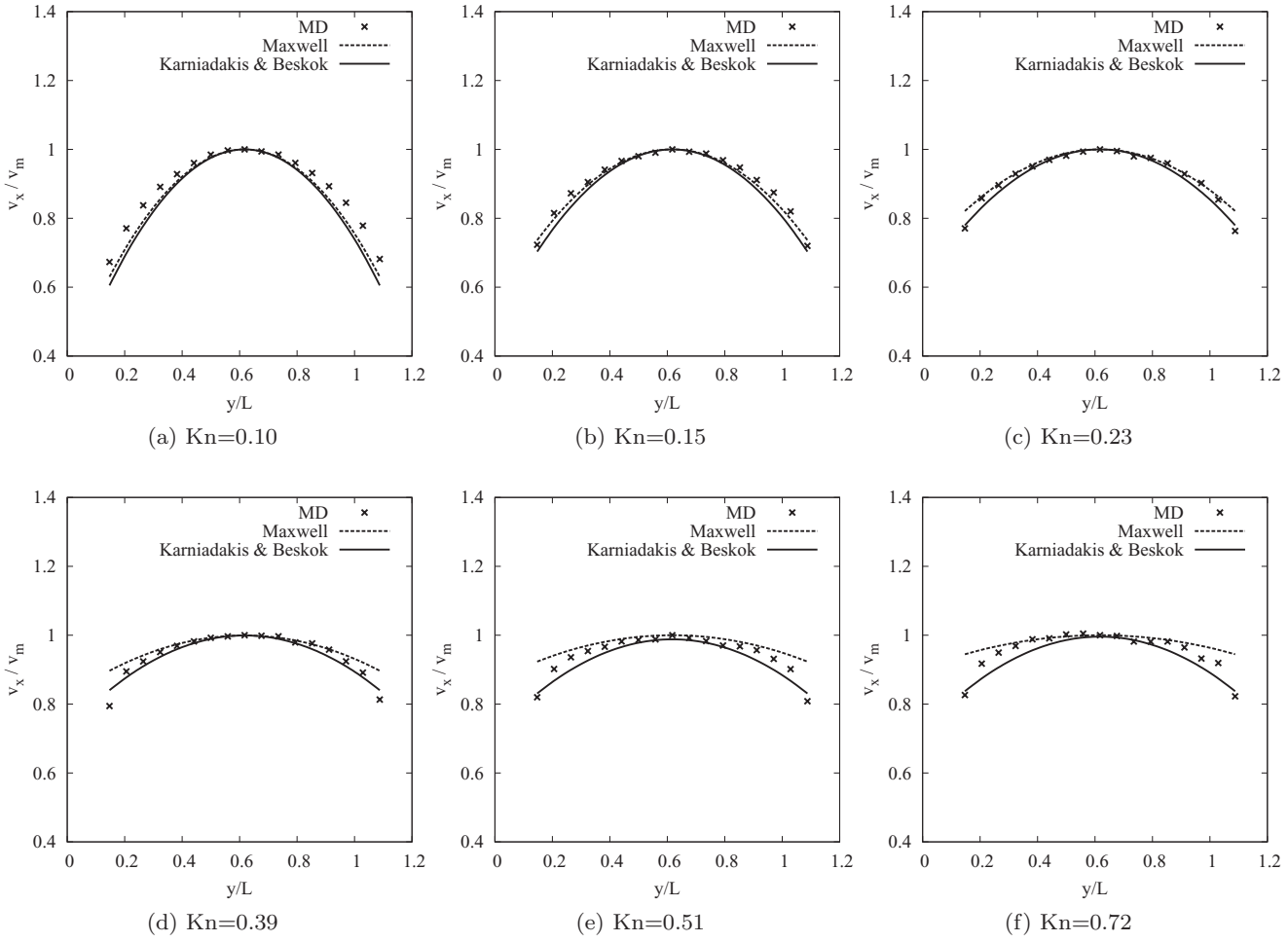

FIG. 14. The comparison of first- and second-order slip models with MD data is shown. The MD data are represented with points and the slip models with lines. The dotted line represents the first-order model and the continuous line the second-order model.

indicating the applicability of the model in the moderately rarefied conditions. The difference between these models is meager at low values of Kn and it becomes more apparent for higher values of Kn. This shows that the second-order term has significant effect only at higher values of Kn. Note that the second-order model predicts the velocity profile near the wall region where nonlinear effects are predominant.

In light of the above results, it is worth discussing the shortcomings of experimental determination of TMAC in nanochannels. In microchannel experiments, the value of C_1 and C_2 are calculated using the value of average velocity obtained from a mass flow rate measurement. Apparently, as far as the Maxwell model is concerned, any change in the value of a leads to different conclusion on the value of TMAC [4]. Furthermore, to the best our knowledge, direct observation of the slip velocity has never been considered in experimental determination of TMAC. According to the results from the present study, although the predicted profiles do not match exactly with the MD data, the average velocities match closely in many cases. Consequently, this is another possible source of error in the calculation of TMAC by experimental means.

The comparison of MD data with the predicted profiles shows several interesting features, such as the value of C_1. The value of C_1 ($\sim$5) lies away from most of the other proposed values by a considerable margin. Accordingly, the assumption of diffuse reflection or $\alpha_x = 1$ is proved unreasonable for smooth surfaces and at moderate rarefaction levels [3,4]. Furthermore, when $\alpha_x < 1$, the value of C_2 has to be negative for predicting the amount of slip accurately. It was speculated in the second-order study that the negative value of C_2 would be significant when $\alpha_x < 1$ [43]. This hypothesis has been proven true in the present study. Further, one can note that the second-order model that predicts the slip velocity accurately associates the term $(2 - \sigma_x)/\sigma_x$ with first- and second-order coefficients. Thus, with the accurate values of ACs, the applicability of the NS equation can be further extended in the transition regime, as demonstrated in the present study.

VI. CONCLUSION

Nonequilibrium molecular-dynamics simulations have been performed to investigate the accommodation coefficients in a nanochannel flow. A platinum-argon system in the slip and early transition regime was considered for this investigation. The Poiseuille flow was simulated by applying an acceleration field to the fluid particles. The gas-surface interaction properties, such as energy and momentum

accommodation coefficients, which determine the amount of slip and temperature jump, were investigated.

The single-particle trajectories showed that the wall retained its structural integrity, which could affect the interaction properties. The standard deviations of the calculated values of ACs were well within the acceptable range, showing the consistency of the calculated values. The system was also studied by varying both the number of gas molecules and the acceleration field. It was seen that the accommodation coefficients decrease with an increase in acceleration field and Kn. Further, it was revealed that the accommodation coefficients approach a limiting value at higher values of gravity and Kn. The study also shows that the collision time has significant effect on EAC.

The calculated values of ACs were used to predict the dimensionless slip length for the Maxwell model, and a linear relationship between the slip length and Kn was predicted. The dimensionless slip length obtained from the velocity profile, which was found to depend on gravity and Kn, was compared with the results obtained from the Maxwell slip model. It is found that the first-order linear slip model accurately predicts the slip length and velocity profile for values of Kn as high as 0.15. Knowing the accurate values of ACs, the applicability of the NS equation can be further extended in the transition regime by employing a second-order slip model. The results obtained from MD calculations are in good agreement with the results from the available experiments and theoretical studies.

[1] S. Colin, *Microfluidics* (Wiley, London, 2010).
[2] B. T. Porodnov, P. E. Suetin, S. F. Borisov, and V. D. Akinshin, J. Fluid Mech. **64**, 417 (1974).
[3] E. B. Arkilic, K. S. Breuer, and M. A. Schmidt, J. Fluid Mech. **437**, 29 (2001).
[4] S. Colin, P. Lalonde, and R. Caen, Heat Transfer Eng. **25**, 23 (2004).
[5] J. Maurer, P. Tabeling, P. Joseph, and H. Willaime, Phys. Fluids **15**, 2613 (2003).
[6] N. Dongari, A. Agrawal, and A. Agrawal, Int. J. Heat Mass Transf. **50**, 3411 (2007).
[7] N. G. Hadjiconstantinou, Microscale Therm. Eng. **9**, 137 (2005).
[8] A. Beskok, Numer. Heat Tr. B-Fund. **40**, 451 (2001).
[9] T. Zhang, L. Jia, and Z. Wang, Int. J. Heat Mass Transf. **51**, 6323 (2008).
[10] W. P. Yudistiawan, S. Ansumali, and I. V. Karlin, Phys. Rev. E **78**, 016705 (2008).
[11] J. S. Hansen, B. D. Todd, and P. J. Daivis, Phys. Rev. E **84**, 016313 (2011).
[12] R. W. Barber and D. R. Emerson, Heat Transfer Eng. **27**, 3 (2006).
[13] L. OHare, D. A. Lockerby, J. M. Reese, and D. R. Emerson, Int. J. Heat Fluid Fl. **28**, 37 (2007).
[14] J. Sun and Z.-X. Li, Mol. Phys. **106**, 2325 (2008).
[15] S. Colin, Microfluid. Nanofluid. **1**, 268 (2005).
[16] B.-Y. Cao, J. Sun, M. Chen, and Z.-Y. Guo, Int. J. Mol. Sci. **10**, 4638 (2009).
[17] J. M. Hailey, *Molecular Dynamics Simulation* (Wiley Interscience, Singapore, 1997).
[18] D. K. Bhattacharya and G. C. Lie, Phys. Rev. Lett. **62**, 897 (1989).
[19] D. K. Bhattacharya and G. C. Lie, Phys. Rev. A **43**, 761 (1991).
[20] G. Arya, H.-C. Chang, and E. J. Maginn, Mol. Simul. **29**, 697 (2003).
[21] J. L. Xu and Z. Q. Zhou, Heat Mass Transfer **40**, 859 (2004).
[22] C. Y. Soong, T. H. Yen, and P. Y. Tzeng, Phys. Rev. E **76**, 036303 (2007).
[23] P. Spijker, A. J. Markvoort, S. V. Nedea, and P. A. J. Hilbers, Phys. Rev. E **81**, 011203 (2010).
[24] S. R. Cook and M. A. Hoffbauer, Phys. Rev. E **58**, 504 (1998).
[25] J. C. Maxwell, Philos. Trans. R. Soc. London **170**, 231 (1879).
[26] C. Cercignani and M. Lampis, Transp. Theory Stat. Phys **1**, 101 (1971).
[27] F. O. Goodman, J. Phys. Chem. Solids **26**, 85 (1965).
[28] R. Logan, Surf. Sci. **15**, 387 (1969).
[29] G. Mo and F. Rosenberger, Phys. Rev. A **44**, 4978 (1991).
[30] J. Koplik, J. R. Banavar, and J. F. Willemsen, Phys. Rev. Lett. **60**, 1282 (1988).
[31] S. Maruyama and T. Kimura, Thermal Sci. Eng. **7**, 63 (1999).
[32] B. Y. Cao, M. Chen, and Z. Y. Guo, Appl. Phys. Lett. **86**, 091905 (2005).
[33] A. J. Markvoort, P. A. J. Hilbers, and S. V. Nedea, Phys. Rev. E **71**, 066702 (2005).
[34] K. Yamamoto, JSME Int. J. Ser. B Fluids Therm. Eng. **45**, 788 (2002).
[35] M. P. Allen and D. J. Tildesley, *Computer Simulation of Liquids* (Oxford University Press, New York, 1994).
[36] H. J. C. Berendsen, J. P. M. Postma, W. F. van Gunsteren, A. DiNola, and J. R. Haak, J. Chem. Phys. **81**, 3684 (1984).
[37] S. J. Plimpton, J. Comp. Phys. **117**, 1 (1995).
[38] W. Humphrey, A. Dalke, and K. Schulten, J. Mol. Graphics **14**, 33 (1996).
[39] V. Chirita, B. A. Pailthorpe, and R. E. Collins, Nucl. Instrum. Methods B **129**, 465 (1997).
[40] D. L. Morris, L. Hannon, and A. L. Garcia, Phys. Rev. A **46**, 5279 (1992).
[41] M. Barisik and A. Beskok, Microfluid. Nanofluid. **11**, 269 (2011).
[42] G. Karniadakis, A. Beskok, and N. R. Aluru, *Microflows and Nanoflows* (Springer, New York, 2005).
[43] A. Beskok, G. E. Karniadakis, and W. Trimmer, J. Fluids Eng. **118**, 448 (1996).